C: Energy Conversion and Storage; Energy and Charge Transport

Phenylated Acene Derivatives as Candidates for Intermolecular Singlet Fission

Xiaopeng Wang, Xingyu Liu, Rithwik Tom, Cameron Cook, Bohdan Schatschneider, and Noa Marom

J. Phys. Chem. C, **Just Accepted Manuscript** • DOI: 10.1021/acs.jpcc.8b12549 • Publication Date (Web): 18 Feb 2019

Phenylated Acene Derivatives as Candidates for Intermolecular Singlet Fission

Xiaopeng Wang,[a] Xingyu Liu,[a] Rithwik Tom,[b] Cameron Cook,[c] Bohdan Schatschneider,[c] and Noa Marom,[a,b,d]*

[a]Department of Materials Science and Engineering, Carnegie Mellon University, Pittsburgh, PA 15213, USA;

[b]Department of Physics, Carnegie Mellon University, Pittsburgh, PA 15213, USA;

[c]Department of Chemistry and Biochemistry, California State Polytechnic University at Pomona, Pomona, CA 91768, USA;

[d]Deparment of Chemistry, Carnegie Mellon University, Pittsburgh, PA 15213, USA

ABSTRACT: Singlet fission (SF), a spin-conserving process where one singlet exciton converts into two triplet excitons, may improve the efficiency of organic photovoltaics. Only a few materials have been experimentally observed to undergo intermolecular SF, most of which are acenes and their derivatives. Using many-body perturbation theory in the *GW* approximation and the Bethe-Salpeter equation (BSE), we systematically investigate the electronic and excitonic properties of tetracene, pentacene, and their phenylated derivatives in the gas phase and solid state. Their potential for SF is evaluated with respect to the thermodynamic driving force and the

singlet exciton charge transfer character. In both the gas phase and solid state, pentacene and its derivatives are more promising than tetracene analogs. Within a family of molecules containing the same acene backbone, increasing the number of phenyl side groups is detrimental for the SF driving force in the gas phase. However, in the solid state, the SF driving force and the exciton character are modulated by intermolecular interactions present within different packing arrangements. Molecules with a higher number of phenyl side groups often form crystals with less cofacial interactions between the acene backbones. These crystals are found to exhibit a higher SF driving force and a higher degree of singlet exciton charge transfer character. In particular, 5,7,12,14-tetraphenylpentacene (TPP), 1,4,6,8,11,13-hexaphenylpentacene (HPP), and 1,2,3,4,6,8,9,10,11,13-decaphenylpentacene (DcPP) emerge as promising candidates for intermolecular SF in the solid state.

1. INTRODUCTION

Organic photovoltaic (OPV) devices have advantages, such as low cost and flexibility,[1-3] however, mass-production and application of OPV devices have been hindered because of their relatively low solar conversion efficiency. Singlet exciton fission (SF), a molecular analogue of multi-exciton generation, could offer an alternative approach to surpass the Shockley-Queisser limit and extend the theoretical efficiency up to 45%.[4-8] SF is a spin conserving four-particle process[9] where one singlet electron-hole pair, or singlet exciton (S_1), is spontaneously converted into two triplet excitons (T_1T_1) localized on two neighboring molecules (intermolecular SF or xSF)[10,11] or on two spatially separated chemical groups in one molecule (intramolecular SF or iSF).[12,13] Because it is spin-forbidden for a triplet electron-hole pair to recombine to the ground state, the lifetime of

triplet excitons is enhanced. This is favorable for harvesting the excitons and thus improving OPV efficiency.[7,14,15]

SF was first discovered in crystalline anthracene in 1965.[16] A number of SF materials have been studied since.[17-25] In particular, crystalline tetracene (TET) and pentacene (PEN) have been extensively examined and discussed due to their high triplet yield, ultrafast transfer between bright and dark states, and foreseeable implementation into optoelectronics.[15,26] These merits make tetracene and pentacene reasonable starting compounds in designing SF materials. Synthesizing their functionalized derivatives could help achieve increased solubility, higher air stability, and more favorable packing arrangements.[27-29] Previous studies of pentacene derivatives, such as bis(triisopropylsilylethynyl) pentacene (TIPS-pentacene) and its aza derivatives have suggested that singlet exciton properties are correlated with π-orbital stacking.[28,30] Moreover, it has been found that nitrogen substitution of aza derivatives may accelerate the triplet state formation process.[28,30,31] SF has also been observed in diphenyl-tetracene (DPT), orthorhombic rubrene (RUB) and diphenyl-pentacene (DPP), all of which are phenylated acene derivatives.[10,18,32,33,34]

SF is a collective many-body quantum mechanical process, whose efficiency depends on multiple factors.[7,9,14,35] The primary descriptor associated with SF is the thermodynamic driving force, E_S-2E_T, where E_S is the energy of the first excited singlet state (corresponding to the optical gap) and E_T is the energy of the lowest excited triplet state.[7-9] A secondary descriptor related to the efficiency of intermolecular SF in the solid state is the degree charge transfer character (%CT), which is the probability of the excited electron and hole to be found on different molecules.[9,35,36] A high %CT of the

singlet exciton could facilitate the coupling between the singlet state and triplet states of neighboring molecules.[8,9,14] Crystal structure can significantly affect the fission rates by changing both the energetics and the exciton wave-functions of the singlet and triplet states.[35,37-39]

The debate regarding which molecular arrangement is more favorable to SF is still ongoing. In this respect, it is instructive to analyze trends in the properties of families of structurally or chemically similar chromophores. Sutton *et al*.[40] studied the impact of molecular packing on SF performance for six rubrene derivatives and found that in π-stacked structures SF may be facilitated by vibronic coupling, whereas in structures that do not display π-stacking, SF may be inefficient due to small coupling between singlet and triplet states. Wang *et al*.[41] performed a systematic comparison among a series of pentacene dimers with different longitudinal and lateral displacements. They showed that switching from cofacial to slip-stacked dimer arrangements results in tenfold increase of SF rate. In contrast, Feng *et al*.[42] have argued that slip-stacking is not the only configuration that presents efficient fission, but that the herringbone (HB) packing motif of tetracene and pentacene is also beneficial to SF performance. This calls for further investigation of the relationship between intermolecular interactions and SF-related properties among chemical families of functionalized chromophores in the solid state.

Here, we investigate a series of phenylated acene derivatives, two with tetracene backbones [5,12-diphenyltetracene (DPT) and rubrene (RUB)] and five with pentacene backbones [6-phenylpentacene (MPP), 6,13-diphenylpentacene (DPP), 5,7,12,14-tetraphenyl-pentacene (TPP), 1,4,6,8,11,13-hexaphenylpentacene (HPP), and 1,2,3,4,6,8,9,10,11,13-decaphenylpentacene (DcPP)], whose structures[43-47] are illustrated

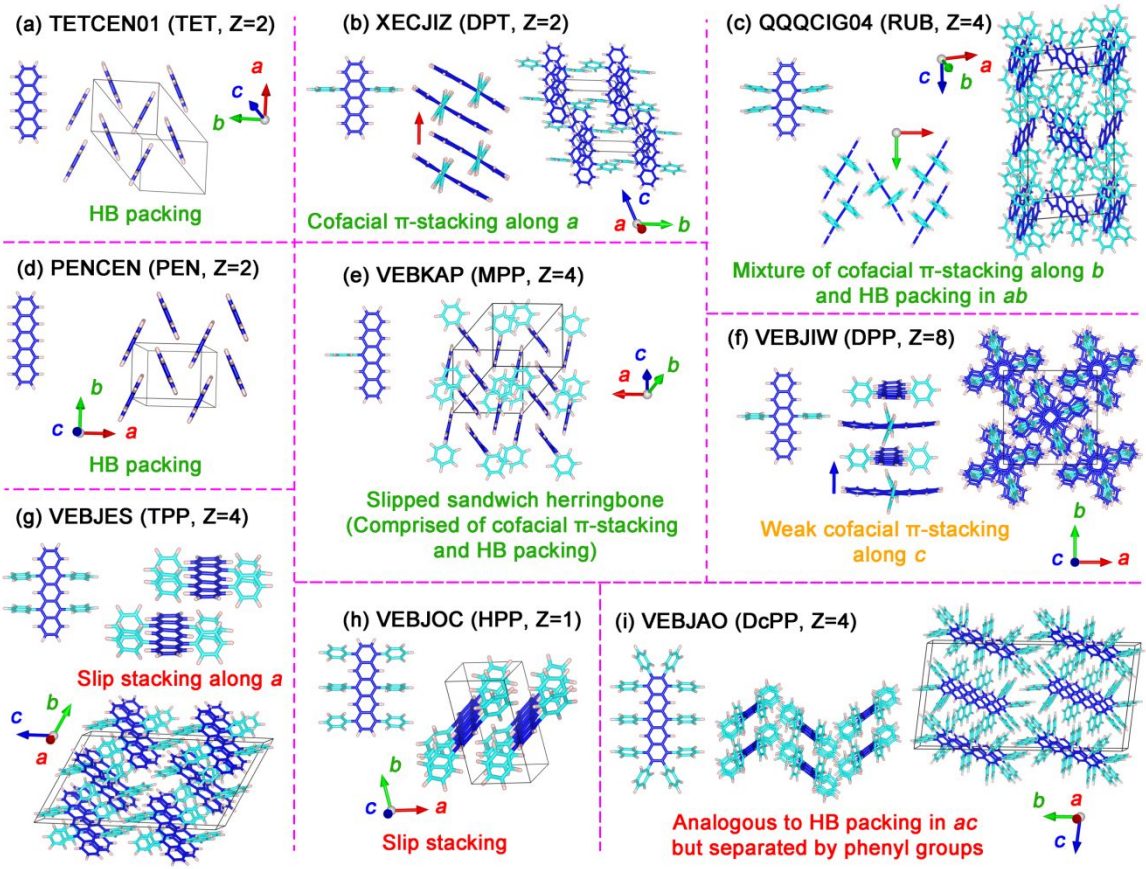

Figure 1. Single molecules, molecular packing and crystal structures of tetracene, pentacene, and their derivatives. The acene backbones are colored in dark blue and the phenyl side groups are colored in light blue. Z indicates the number of molecules per unit cell. The corresponding CSD entries are TETCEN01,[43] XECJIZ,[44] QQQCIG04,[45] PENCEN,[46] VEBKAP,[47] VEBJIW,[47] VEBJES,[47] VEBJOC,[47] and VEBJAO.[47]

in Figure 1. While tetracene and pentacene crystallize in a HB structure,[39,48-52] their phenylated derivatives display a rich variety of packing arrangements (Hirshfeld surface analyses of these structures are provided in the Supporting Information). Due to the presence of the phenyl side groups, DPT does not present a HB packing motif but forms π-stacks characterized by cofacial intermolecular interactions (also known as β-HB).[48,49] Orthorhombic rubrene displays a combination of cofacial π-stacking along the *b*-direction and HB packing in the *ab*-plane.[35,48,49] MPP crystallizes in a "slipped" sandwich herringbone (SHB) structure with a mixture of cofacial and HB packing, as shown in the

Supporting Information. In DPP, the molecules are stacked along the *c*-direction, however, their backbone orientation alternates, such that neighboring molecules lie perpendicular to each other in the *ab*-plane. With the addition of more phenyl side groups, the backbones of TPP, HPP and DcPP are increasingly separated from each other.[47] Both TPP and HPP do not show any cofacial interactions between the pentacene backbones and in the HB-like structure of DcPP, the pentacene backbones are more than 5 Å apart.

We use many-body perturbation theory (MBPT) within the *GW* approximation and the Bethe-Salpeter equation (*GW*+BSE)[23,53-55] to study the electronic and optical properties of tetracene, pentacene, and their phenylated derivatives in the gas phase and solid state. We elucidate the effect of crystal packing and explain the origin of the differences between the trends found in isolated molecules vs. molecular crystals. To assess the likelihood of intermolecular SF in the solid state for the materials studied here, we use a two-dimensional descriptor based on the thermodynamic driving force for SF (E_S-$2E_T$) and the degree of singlet exciton charge transfer character (%CT). We find that weak cofacial interactions or slip stacking may be beneficial for the SF performance of phenylated acene derivatives. In particular, TPP, HPP, and DcPP emerge as promising new candidate materials for intermolecular SF in the solid state.

2. METHODOLOGY

The geometries of all the single molecules were optimized using density functional theory (DFT) with the generalized gradient approximation of Perdew, Burke, and Ernzerhof (PBE)[56,57] coupled to the Tkatchenko-Scheffler (TS) pairwise dispersion method[58] implemented in the all-electron numerical atom-centered orbital (NAO) code, FHI-

aims.[59-61] In the gas phase, rubrene adopts a conformation with a twisted backbone.[62,63] However, here we calculated the properties of a rubrene molecule with a planar backbone because this is the conformation found in the crystal structure. The *GW* and Bethe-Salpeter equation (BSE) calculations isolated molecules were performed with FHI-aims using aug2tier2 basis sets. The non-self-consistent G_0W_0 method was employed to compute the quasiparticle eigenvalues of single molecule orbitals using the mean-field PBE calculation as a starting point. Based on a previous benchmark study,[64] for polycyclic aromatic hydrocarbons containing only C and H atoms the PBE functional is a sufficiently accurate starting point for G_0W_0 calculations, in the sense that it predicts the correct orbital ordering and the resulting spectrum is qualitatively similar to spectra obtained using more accurate methods and to experiments. Similar trends were found for rubrene, perylene, and quaterrylene.[35,39] G_0W_0@PBE is therefore sufficiently accurate for the purpose of qualitative comparisons between the molecules studied here.

The single molecule optical gaps were obtained through BSE within the Tamm-Dancoff approximation (TDA),[65] which has been shown to improve the accuracy of the triplet excitation energies relative to higher level theories, such as coupled cluster with singles, doubles, and perturbative triples (CCSD(T))[66,67] (a screening mixing strategy[68,69] may also improve the accuracy of the triplet energy, however it is not used here). However, the effect of TDA on singlet energy is still under debate.[66,67] 30 occupied states and 30 unoccupied states were considered for the BSE calculation. In the Supporting Information, *GW* and BSE results of single molecules obtained from FHI-aims are compared to those from the BerkeleyGW code,[65] and experimental data. Due to the

systematic underestimation of the G_0W_0 gap and BSE excitation energies compared to the experiments, we restrict our discussion to qualitative trends among different molecules.

The starting geometries of crystalline tetracene, pentacene, and their derivatives studied here were obtained from the Cambridge Structural Database (CSD), whose reference codes are provided in Figure 1. The geometries were then optimized with the CASTEP code[70] using PBE coupled to TS. Norm-conserving pseudopotentials were utilized for C and H atoms. The planewave basis set cut-off was 750 eV and the k-point grid spacing was 0.07 $Å^{-1}$. The convergence criteria for the total energy, maximum force, maximum stress, and maximum displacement were 5×10^{-6} eV/atom, 0.01 eV/Å, 0.02 GPa, and 5×10^{-4} $Å^{-1}$, respectively.

The single-point calculations of electronic and optical properties of crystalline tetracene, pentacene, and their derivatives were performed with *GW* and BSE implemented in the BerkeleyGW code.[65] The convergence of the numerical settings for such calculations has been discussed and carefully benchmarked previously.[35,39] Therefore, only a brief description of the system dependent settings is provided here. Firstly, the DFT eigenvectors and eigenvalues were generated with Quantum Espresso,[71] using the PBE functional and norm-conserving pseudopotentials. K-grids of 4×4×2, 4×2×2, 2×2×1, 4×4×2, 2×2×2, 3×3×3, 4×2×1, 4×2×2, and 2×2×1 were used for crystalline TET, DPT, RUB, PEN, MPP, DPP, TPP, HPP, and DcPP, respectively. Secondly, G_0W_0 quasiparticle band structures were computed using the dielectric function and self-energy operator constructed by summing over 550 conduction bands for all the crystals. The static remainder correction[72] was applied to accelerate the convergence with

respect to the number of conduction bands. The energy cut-off for the calculation of the polarizability was set to 10 Ry.

Lastly, optical excitations were calculated by solving the BSE within the Tamm-Dancoff approximation (TDA)[65] using 24 valence bands and 24 conduction bands. Because of the slow convergence behaviour of the BSE calculation, denser k-grids were used for this step, of 8×8×4, 8×4×4, 10×10×5, 8×8×4, 4×4×4, 6×6×8, 8×4×2, 8×4×4, and 20×4×1 for TET, DPT, RUB, PEN, MPP, DPP, TPP, HPP, and DcPP, respectively. The exciton wave-functions were calculated by fixing the hole position at a high hole probability site.[39] In some cases, converging the exciton wave-function, such that it was entirely contained in the simulation cell, required highly extended super-cells along the molecular packing direction, as discussed in the Supporting Information. For example, for DPP, 8 unit cells (32 molecules) were used along the *c*-direction. The degree of charge transfer character (%CT), which describes the probability of the electron and hole of an

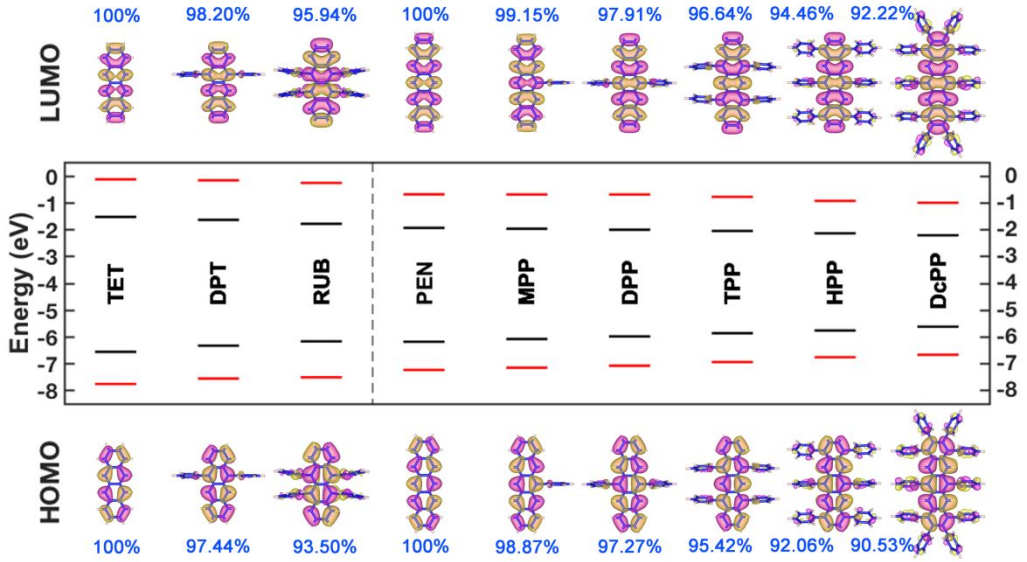

Figure 2. G_0W_0@PBE quasiparticle energies of the HOMO-1 (red), HOMO (black), LUMO (black), and LUMO+1 (red) of tetracene, pentacene, and their phenylated derivatives. The HOMO and LUMO of each molecule are visualized. The percent of frontier orbital charge contributed by the acene backbone, based on Bader analysis, is shown in blue.

exciton residing on different molecules, were computed using the double-Bader analysis (DBA) method, developed by us.[39] Briefly, DBA extends the Bader charge partitioning scheme to exciton wave-functions with two spatial coordinates by performing nested sums over electron and hole positions.

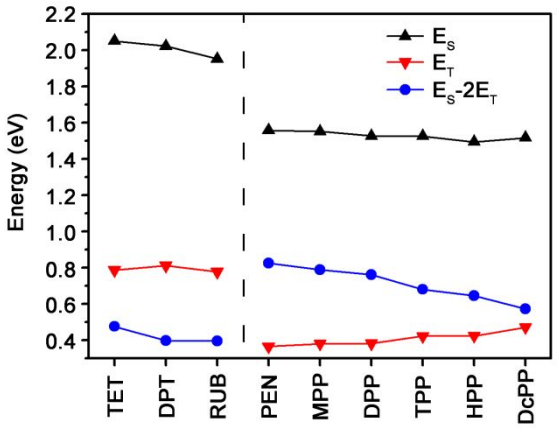

Figure 3. Singlet (black) and triplet (red) excitation energies and thermodynamic driving force for SF (blue) calculated from G_0W_0+BSE@PBE method for each molecule.

3. RESULTS AND DISCUSSION

3.1 Single Molecules

We begin by investigating the effect of phenyl substitution on the molecular properties of tetracene and pentacene derivatives. Figure 2 shows the G_0W_0@PBE quasiparticle energies of the HOMO, HOMO-1, LUMO, and LUMO+1. Visualizations of the HOMO and LUMO are also shown. Based on Bader analysis,[73] more than 90% of the frontier orbital charge density is located on the acene backbones. Although the phenyl groups do not contribute significantly to the frontier orbitals, their presence leads to a decrease in the HOMO-LUMO gap, possibly due to increased electronic screening. The single molecule quasiparticle gap decreases from 5.02 eV in tetracene through 4.69 eV in DPT to 4.38 eV in rubrene in agreement with Ref. 63. The same trend holds in pentacene derivatives. The HOMO energy increases and LUMO energy decreases, narrowing the gap from 4.24 eV in pentacene to 3.41 eV in DcPP. The phenyl groups contribute

additional peaks in the deeper valence region of the G_0W_0@PBE quasiparticle spectra, as shown in Figure S2 of the Supporting Information.

Figure 3 shows the singlet and triplet excitation energies of the tetracene and pentacene derivatives, obtained from G_0W_0+BSE@PBE, as well as the thermodynamic driving force for SF (tabulated values are provided in the Supporting Information). The optical gap, E_S, does not decrease as much as the fundamental gap with the number of phenyl groups because the additional screening contributed by the phenyl groups reduces the singlet exciton binding energy (BE_S).[74] We find that pentacene with a larger molecule size has a smaller E_T than tetracene, in agreement with Ref. 24. Similar to E_S, E_T is the difference between the GW fundamental gap and the triplet exciton binding energy (BE_T). BE_T is typically significantly larger than BE_S, owing to the absence of the repulsive exchange electron-hole interaction. BE_T decreases with the number of phenyl groups, similar to the fundamental gap and BE_S, such that overall E_T remains almost constant for the tetracene series and increases slightly for the pentacene series with the addition of phenyl side groups (see further discussion in the Supporting Information). Consequently, the thermodynamic driving force for SF, E_S-$2E_T$, generally decreases with the number of phenyl rings for both the tetracene and pentacene series.

Within the oligoacene family, the thermodynamic driving force for SF has been shown to increase with molecule size.[24] Pentacene with a high E_S-$2E_T$ is currently the best-known SF material. Anthracene, with smaller E_S-$2E_T$, and its derivative diphenylanthracene (DPA), are known to exhibit triplet-triplet annihilation (TTA), the reverse process of SF.[75-77] Tetracene, with E_S-$2E_T$ value in between pentacene and anthracene, is less efficient than pentacene in terms of SF. Furthermore, both SF and TTA

have been observed in the tetracene derivative, rubrene.[18,76] The magnitude of E_S-$2E_T$ thus appears to be primarily determined by the size of the acene backbone, and only slightly modulated by the phenyl side groups. Functionalization with side groups may be a useful strategy to optimize device performance by tuning the molecular properties, including the optical absorption threshold, the exciton binding energy, the ionization potential (IP), the electron affinity (EA), and consequently the energy level alignment at functional interfaces.

3.2 Molecular Crystals

The electronic and optical properties of molecular crystals depend not only on the molecular properties, but also on the electronic coupling between neighboring molecules. Although the phenyl groups do not contribute significantly to the frontier molecular orbitals, they affect the solid-state properties by altering the crystal packing, as shown in Figure 1. The G_0W_0@PBE quasiparticle band structures of crystalline phenylated tetracene and pentacene derivatives are shown in Figure 4. Crystals with HB packing

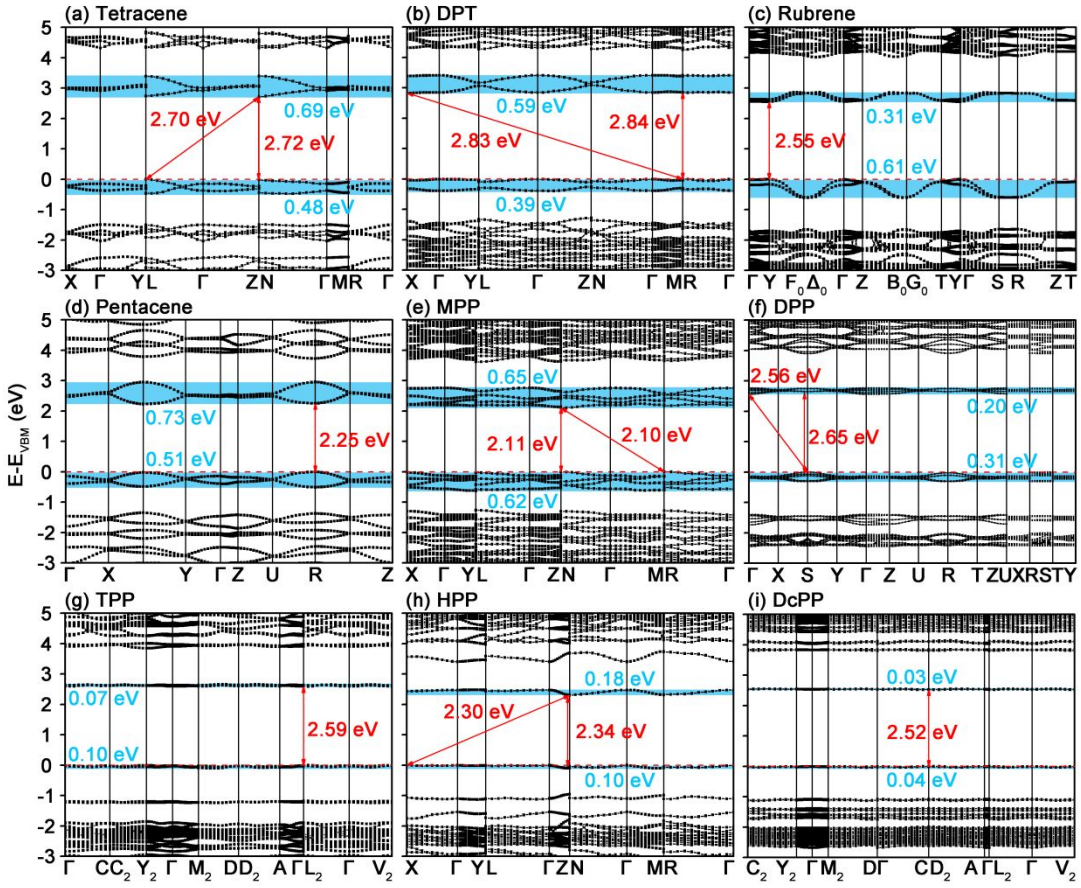

Figure 4. G_0W_0@PBE quasiparticle band structures of crystalline tetracene, pentacene, and their phenylated derivatives. The valence band maximum (VBM) is shifted to 0 eV. Direct and indirect band gaps are indicated in red. HOMO and LUMO derived band dispersions are indicated in blue (there are as many HOMO and LUMO derived bands as the number of molecules in the primitive unit cell).

motifs and/or with significant cofacial intermolecular interactions are characterized by dispersed bands, as seen for tetracene, DPT, rubrene, pentacene, and MPP in panels (a)-(e). The DPP crystal exhibits less band dispersion, as seen in panel (f). This may be attributed to the weak cofacial interactions between neighboring molecules stacked along the *c*-direction, whose backbones are perpendicular to each other in the *ab* plane, as seen in Figure 1f. Moreover, the distance between cofacially stacked backbones in DPP is about 5 Å,[47] significantly larger than *e.g.,* 3.8 Å in DPT. The TPP, HPP, and DcPP crystals exhibit nearly flat bands, as shown in panels (g), (h), and (i) of Figure 4, respectively. For these molecules, multiple phenyl side groups create a considerable steric barrier preventing the overlap of frontier orbitals, localized on the backbones. In the TPP and HPP crystals, the molecules are slip-stacked, such that the side groups of one molecule interact with the backbone of another, as shown in panels (g) and (h) of Figure 1. In the DcPP crystal, despite the HB-like packing in the *ac* plane, the phenyl groups spatially separate pentacene backbones apart by more than 5 Å, leading to minimal electronic coupling between the frontier orbitals.

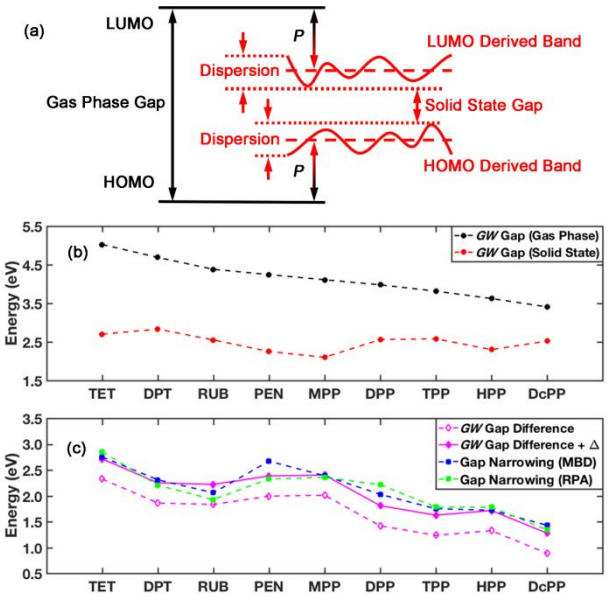

Figure 5. (a) Schematic of gap narrowing from the gas phase to the solid state. (b) G_0W_0@PBE gas phase gap from FHI-aims (black) and solid state band gap from BerkeleyGW (red). (c) G_0W_0@PBE gap difference between gas phase and solid state with (solid magenta) and without (dashed magenta) a correction of 0.4 eV. The gap narrowing is calculated from eq 1 with the static polarizability obtained from MBD (blue) and RPA (green).

In addition to band dispersion, another important contribution to the difference between the properties of isolated molecules and molecular crystals is the narrowing of the fundamental gap due to polarization effects.[74,78-80] As shown in Figures 2 and 5, the gas phase HOMO-LUMO gap decreases monotonically with the number of phenyl groups. Interestingly, the fundamental band gaps in the solid state do not follow the same trend, and even increase for the larger phenylated pentacene derivatives, as shown in Figures 4 and 5. This difference is primarily attributed to the enhanced dielectric screening and band dispersion in the crystalline environment. As illustrated in Figure 5a, we estimate the gap narrowing by:

$$E_{narrowing}^{gap} = 2P + \frac{E_{disp}^{v} + E_{disp}^{c}}{2} \qquad (1)$$

where $E_{narrowing}^{gap}$ is the gap narrowing from gas phase to solid state, E_{disp}^{v} is the dispersion of the HOMO derived valence bands, E_{disp}^{c} is the dispersion of the LUMO derived conduction bands, and P is the stabilization energy of an ionized molecule due to the dielectric screening by the surrounding molecules in the solid state. The screening effect reduces the solid-state band gap by $2P$ because the ionization energy is decreased by P, while the electron affinity is increased by P. The polarization energy is calculated from a simple electrostatic model:[81,82]

$$P = -e^{2}\frac{\varepsilon - 1}{2R\varepsilon} \qquad (2)$$

In this model the ionized molecule is approximated as a hollow sphere of radius R, which is given by:

$$R = \left(\frac{3V}{4\pi N}\right)^{\frac{1}{3}} \qquad (3)$$

where V/N is the volume per molecule in the primitive cell. The dielectric constant, ε, in eq 2 is calculated from the Clausius-Mossotti relation:

$$\frac{\varepsilon - 1}{\varepsilon + 2} = \frac{4\pi}{3V}\alpha \qquad (4)$$

where α is the static polarizability. The polarizability may be calculated either by using DFT with the many-body dispersion (MBD)[78-80] method or within many-body perturbation theory via the random-phase approximation (RPA).[74] The two methods give comparable results of gap narrowing, as shown in Figure 5c, with the largest difference being 0.34 eV for pentacene. The polarization energies for pentacene obtained from MBD and RPA are, respectively, 1.18 and 1.01 eV, in agreement with 1.00/1.12 eV for HOMO/LUMO in Ref. 83.

Finally, a correction, Δ, may be added to account for the fact that the gas phase and solid state gaps are calculated here using different codes. As shown in the Supporting Information and in Ref. 84, the *GW* gaps obtained from FHI-aims are typically a few hundred meV smaller than those obtained from BerkeleyGW. For example, the HOMO-LUMO *GW* gap of an isolated tetracene molecule produced by FHI-aims is 0.4 eV less than the gap produced by BerkeleyGW. A detailed discussion of the origins of the discrepancies between different *GW* implementations is provided in Ref. 84. Briefly, the difference may be attributed primarily to the use of pseudo-potentials and the generalized

plasmon pole approximation in BerkeleyGW. Although this difference varies slightly for different molecules, we use a rigid shift of $\Delta = 0.4$ eV in Figure 5c.

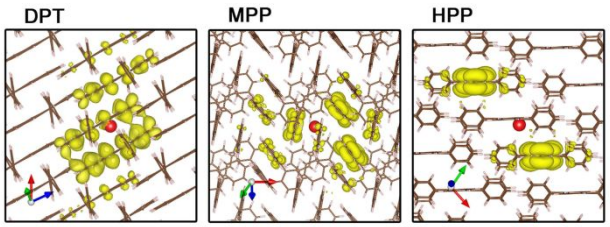

Figure 6. Lowest energy singlet exciton wavefunctions. Red spheres indicate hole positions. Electron probability densities are shown in yellow.

As shown in Figure 5, the simplistic model given by eq 1 quantitatively captures the trend in the quasiparticle gap differences between the gas phase and solid state for the phenylated acene series. Hence, the gap narrowing from single molecules to molecular crystals may be explained by the combined effect of the enhanced dielectric screening in the solid state and the electronic coupling between the frontier orbitals of neighboring molecules. The former decreases the HOMO-LUMO energy gap by twice the polarization energy. The latter further narrows the gap by dispersing the HOMO and LUMO derived bands (additional details are provided in the Supporting Information).

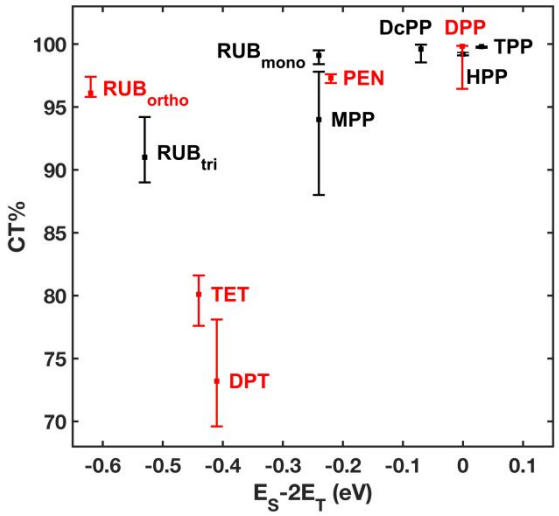

Figure 7. SF driving force (E_S-2E_T) on the x-axis and degree of singlet exciton charge transfer character (%CT) on the y-axis for the nine crystals in Figure 1 with two additional metastable rubrene polymorphs, monoclinic (QQQCIG13) and triclinic (QQQCIG14).[85] Error bars represent the minimal and maximal values of %CT obtained from DBA with different hole positions. The materials where SF has been observed experimentally are indicated in red. Singlet and triplet excitation energies and values of E_S-2E_T and %CT are tabulated in Table S5 of the Supplementary Information.

The crystal packing affects not only the band structure and excitation energies, but

also the character of exciton wave-functions.[35,39] The electron probability distribution is typically localized primarily on the molecules that have the strongest electronic coupling with the molecule on which the hole resides.[39] Representative examples of singlet exciton wave-functions are shown in Figure 6 (additional singlet and triplet exciton wave-functions are plotted in the Supporting Information). When there is a cofacial π-stacking direction, as in the case of DPT and DPP, the singlet exciton wave function is distributed along this direction. In the slipped SHB packing of MPP, the electron probability is distributed on several neighbors with strong electronic coupling within the molecular layer of the molecule with the hole. In slip-stacked structures, such as TPP, HPP, and DcPP, the electron is localized on two slip-stacked neighbors with relatively large electronic coupling to the molecule with the hole. Singlet excitons in such weakly coupled structures tend to have a high degree of charge transfer character. In all the materials studied here, the triplet excitons have a more Frenkel-like character with the electron distribution concentrated mainly on the same molecule as the hole, as shown in the Supporting Information.

In Figure 7, the phenylated tetracene and pentacene crystals are ranked with respect to a two-dimensional descriptor based on the thermodynamic driving force for SF, E_S-$2E_T$, and the degree of singlet exciton charge transfer character, %CT.[38] E_S-$2E_T$ is systematically underestimated, owing to the limitations of the *GW*+BSE approach, as discussed in Refs. 35, 39, 86-88. Therefore, we restrict the discussion to qualitative trends. Overall, E_S-$2E_T$ and %CT are higher for the phenylated pentacene crystals than the phenylated tetracene crystals. This indicates that the thermodynamic driving force for SF depends strongly on the backbone length, which is consistent with our findings for

isolated molecules. However, a variation up to 0.4 eV in E_S-$2E_T$ is found within each group. Interestingly, for the phenylated acene crystals E_S-$2E_T$ does not decrease with the number of phenyl side groups in contrast to the trend found for isolated molecules in Figure 3. This may be attributed to the effect of crystal packing, with some packing arrangements being more favorable for SF.

Among the pentacene derivatives, MPP in SHB-like packing has a comparable E_S-$2E_T$ to pentacene in HB packing, but a somewhat lower %CT. DPP, TPP, HPP, and DcPP, whose crystal structures are characterized by weak cofacial (π···π) interactions or slip stacking, have higher E_S-$2E_T$ values than pentacene and very high %CT. Among the tetracene derivatives, the orthorhombic and triclinic[35,85] forms of rubrene, whose structures are characterized by cofacial interactions between π-stacked molecules, have a lower E_S-$2E_T$ and higher %CT than HB-packed tetracene. DPT, with less cofacial interactions than orthorhombic and triclinic rubrene, has a comparable E_S-$2E_T$ value to tetracene, but a lower %CT. Monoclinic rubrene,[35,85] whose slip-stacked crystal structure is similar to that of TPP and HPP, stands out in its particularly high E_S-$2E_T$ value, comparable to MPP, as well as a very high %CT. We therefore conclude that slip-stacking and other packing arrangements with weak cofacial intermolecular interactions between the acene backbones may be favorable for intermolecular SF in crystalline acene derivatives, in agreement with the findings of Refs. 41, 42. In particular, TPP, HPP, and DcPP emerge as promising candidates for SF. This may motivate further experimental and theoretical studies of SF in these materials.

4. CONCLUSIONS

In summary, we have studied the electronic and excitonic properties of tetracene, pentacene, and their phenylated derivatives in both the gas phase and solid state, using *GW*+BSE. The phenyl side groups do not contribute significantly to the single molecule frontier orbitals, which are localized mainly on the acene backbones. However, phenyl substitution leads to a monotonic decrease in the gas phase quasiparticle gap due to the increased electronic screening. Unlike the HOMO-LUMO gap in the gas phase, the band gap in the solid state is affected by intermolecular interactions. Two effects contribute to band gap narrowing in the solid state: First, the polarization energy due to the dielectric screening decreases the ionization energy and increases the electron affinity. Second, band dispersion resulting from electronic coupling between the frontier orbitals of neighboring molecules contributes to further gap narrowing. The band dispersion is typically more significant in crystals with HB packing motifs and/or strong cofacial intermolecular interactions. As a result of these effects, the band gap does not decrease monotonically with the number of phenyl side groups and even increases, owing to the weaker cofacial interactions between molecules with a larger number of side groups.

The excitonic properties of isolated molecules and molecular crystals also exhibit significantly different trends with the number of phenyl side groups. The thermodynamic driving force for SF, E_S-$2E_T$, is determined primarily by the size of the acene backbone in both the gas phase and solid state. Overall, E_S-$2E_T$ is higher for phenylated pentacene derivatives than phenylated tetracene derivatives. In isolated molecules, the thermodynamic driving force for SF generally decreases with the number of phenyl rings for both the tetracene and pentacene series. In contrast, a dependence of E_S-$2E_T$ on packing motifs is found in crystals. In both the tetracene and pentacene series, the

phenylated derivatives, whose crystal structures are characterized by weak cofacial interactions or slip stacking, have larger E_S-$2E_T$ than those with HB, cofacial, or SHB packing. Specifically, DPP, TPP, HPP, and DcPP crystals are favorable for SF in terms of both the thermodynamic driving force and the degree of singlet exciton charge transfer character. Three of these materials, TPP, HPP, and DcPP, have not been investigated experimentally as of yet.

Thus, using *GW*+BSE, we have elucidated the effect of crystal packing and explained the origin of the different trends in the gas phase and solid-state properties of phenylated acene derivatives. Based on our findings, studies of isolated molecules or molecular clusters may have limited predictive power with respect to the properties of extended systems. Finally, we have identified TPP, HPP, and DcPP as promising new candidates for intermolecular SF in the solid state.

ASSOCIATED CONTENT

Supporting Information

The Supporting Information is available free of charge on the ACS Publications website.

Single molecule G0W0+BSE@PBE results, PBE band structures of crystals with and without phenyl side groups, exciton wave-functions, singlet and triplet excitation energies, and Hirshfeld surfaces (PDF)

AUTHOR INFORMATION

Corresponding Author

*E-mail: nmarom@andrew.cmu.edu

Notes

The authors declare no competing financial interest.

ACKNOWLEDGMENTS

We thank Volker Blum and Chi Liu from Duke University for helpful discussions of the BSE implementation in FHI-aims. Work at CMU was funded by the Charles E. Kaufman Foundation through grant KA2017-91789 and by the Air Force Office of Scientific Research (AFOSR) through grant FA9550-18-1-0248. Work at CPP was funded by the National Science Foundation (NSF) Division of Materials Research through Grant No. DMR-1637026. This research used resources of the Argonne Leadership Computing Facility (ALCF), which is a DOE Office of Science User Facility supported under Contract No. DE-AC02-06CH11357, and of the National Energy Research Scientific Computing Center (NERSC), a DOE Office of Science User Facility supported by the Office of Science of the U.S. Department of Energy under Contract No. DE-AC02-05CH11231.

REFERENCES

1 Kippelen, B; Brédas, J.-L. Organic photovoltaics. *Energy Environ. Sci.* **2009,** 2, 251–261.

2 Yu, J.; Zheng, Y.; Huang, J. Towards high performance organic photovoltaic cells: a review of recent development in organic photovoltaics. *Polymers* **2014,** 6, 2473–2509.

3 Su, Y.-W.; Lan, S.-C.; Wei, K.-H. Organic photovoltaics. *Mater. Today* **2012,** 15, 554–562.

4 Shockley, W.; Queisser, H. J. Detailed balance limit of efficiency of *p-n* junction solar cells. *J. Appl. Phys*. **1961,** 32, 510–519.

5 Hanna, M. C.; Nozik, A. J. Solar conversion efficiency of photovoltaic and photoelectrolysis cells with carrier multiplication absorbers. *J. Appl. Phys*. **2006,** 100, 074510.

6 Walker, B. J.; Musser, A. J.; Beljonne, D.; Friend, R. H. Singlet exciton fission in solution. *Nat. Chem.* **2013,** 5, 1019–1024.

7 Smith, M. B.; Michl, J. Recent advances in singlet fission. *Annu. Rev. Phys. Chem*. **2013,** 64, 361–386.

8 Casanova, D. Theoretical modelling of singlet fission. *Chem. Rev.* **2018,** 118, 7164–7207.

9 Monahan, N.; Zhu, X.-Y. Charge transfer-mediated singlet fission. *Annu. Rev. Phys. Chem*. **2015,** 66, 601–618.

10 Yost, S. R.; Lee, J.; Wilson, M. W. B.; Wu, T.; McMahon, D. P.; Parkhurst, R. R.; Thompson, N. J.; Congreve, D. N.; Rao, A.; Johnson, K.; et al. A transferable model for singlet-fission kinetics. *Nat. Chem*. **2014,** 6, 492–497.

11 Tamura, H.; Huix-Rotllant, M.; Burghardt, I.; Olivier, Y.; Beljonne, D. First-principles quantum dynamics of singlet fission: coherent versus thermally activated mechanism governed by molecular π stacking. *Phys. Rev. Lett*. **2015,** 115, 107401.

12 Zirzlmeier, J.; Casillas, R.; Reddy, S. R.; Coto, P. B.; Lehnherr, D.; Chernick, E. T.; Papadopoulos, I.; Thoss, M.; Tykwinski, R. R.; Guldi, D. M. Solution-based intramolecular singlet fission in cross-conjugated pentacene dimers. *Nanoscale* **2016,** 8, 10113–10123.

13 Busby, E.; Xia, J.; Wu, Q.; Low, J. Z.; Song, R.; Miller, J. R.; Zhu, X.-Y.; Campos, L. M.; Sfeir, M. Y. A design strategy for intramolecular singlet fission mediated by charge-transfer states in donor-acceptor organic materials. *Nat. Mater*. **2015,** 14, 426–433.

14 Smith, M. B.; Michl, J. Singlet fission. *Chem. Rev*. **2010,** 110, 6891–6936.

15 Congreve, D. N.; Lee, J.; Thompson, N. J.; Hontz, E.; Yost, S. R.; Reusswig, P. D.; Bahlke, M. E.; Reineke, S.; Voorhis, T. Van; Baldo, M. A. External quantum efficiency above 100% in a singlet-exciton-fission–based organic photovoltaic cell. *Science* **2013,** 340, 334–337.

16 Singh, S.; Jones, W. J.; Siebrand, W.; Stoicheff, B. P.; Schneider, W. G. Laser generation of excitons and fluorescence in anthracene crystals. *J. Chem. Phys*. **1965,** 42, 330–342.

17 Zimmerman, P. M.; Zhang, Z.; Musgrave, C. B. Singlet fission in pentacene through multi-exciton quantum states. *Nat. Chem*. **2010,** 2, 648–652.

18 Ma, L.; Zhang, K.; Kloc, C.; Sun, H.; Michel-Beyerle, M. E.; Gurzadyan, G. G. Singlet fission in rubrene single crystal: direct observation by femtosecond pump-probe spectroscopy. *Phys. Chem. Chem. Phys*. **2012,** 14, 8307–8312.

19 Lee, J.; Bruzek, M. J.; Thompson, N. J.; Sfeir, M. Y.; Anthony, J. E.; Baldo, M. A. Singlet exciton fission in a hexacene derivative. *Adv. Mater*. **2013,** 25, 1445–1448.

20 Chan, W. L.; Ligges, M.; Jailaubekov, A.; Kaake, L.; Miaja-Avila, L.; Zhu, X.-Y. Observing the multiexciton state in singlet fission and ensuing ultrafast multielectron transfer. *Science* **2011,** 334, 1541–1545.

21 Johnson, J. C.; Nozik, A. J.; Michl, J. High triplet yield from singlet fission in a thin film of 1,3-diphenylisobenzofuran. *J. Am. Chem. Soc*. **2010,** 132, 16302–16303.

22 Burdett, J. J.; Bardeen, C. J. Quantum beats in crystalline tetracene delayed fluorescence due to triplet pair coherences produced by direct singlet fission. *J. Am. Chem. Soc*. **2012,** 134, 8597–8607.

23 Sharifzadeh, S. Many-body perturbation theory for understanding optical excitations in organic molecules and solids. *J. Phys.: Condens. Matter* **2018,** 30, 153002.

24 Rangel, T.; Berland, K.; Sharifzadeh, S.; Brown-Altvater, F.; Lee, K.; Hyldgaard, P.; Kronik, L.; Neaton, J. B. Structural and excited-state properties of oligoacene crystals from first principles. *Phys. Rev. B* **2016,** 93, 115206.

25 Refaely-Abramson, S.; da Jornada, F. H.; Louie, S. G.; Neaton, J. B. Origins of singlet fission in solid pentacene from an *ab initio* Green's function approach. *Phys. Rev. Lett*. **2017,** 119, 267401.

26 Zimmerman, P. M.; Bell, F.; Casanova, D.; Head-Gordon, M. Mechanism for singlet fission in pentacene and tetracene: from single exciton to two triplets. *J. Am. Chem. Soc*. **2011,** 133, 19944–19952.

27 Anthony, J. E.; Brooks, J. S.; Eaton, D. L.; Parkin, S. R. Functionalized pentacene: improved electronic properties from control of solid-state order. *J. Am. Chem. Soc.* **2001,** 123, 9482–9483.

28 Sharifzadeh, S.; Wong, C. Y.; Wu, H.; Cotts, B. L.; Kronik, L.; Ginsberg, N. S.; J. B. Neaton, Relating the physical structure and optoelectronic function of crystalline TIPS-pentacene. *Adv. Funct. Mater.* **2015,** 25, 2038–2046.

29 Fu, Y.; Zhang, J.; Zeng, T.; Huang, Z.; Cao, W. The synthesis and properties study of 6,13-diphenylpentacene. *Chin. Sci. Bull*. **2008,** 53, 2607–2611.

30 Herz, J.; Buckup, T.; Paulus, F.; Engelhart, J. U.; Bunz, U. H. F.; Motzkus, M. Unveiling singlet fission mediating states in TIPS-pentacene and its AZA derivatives. *J. Phys. Chem. A* **2015,** 119, 6602–6610.

31 Herz, J.; Huckup, T.; Paulus, F.; Engelhart, J.; Bunz, U. H. F.; Motzkus, M. Acceleration of singlet fission in an aza-derivative of TIPS-pentacene. *J. Phys. Chem. Lett*. **2014,** 5, 2425–2430.

32 Roberts, S. T.; McAnally, R. E.; Mastron, J. N.; Webber, D. H.; Whited, M. T.; Brutchey, R. L.; Thompson, M. E.; Bradforth, S. E. Efficient singlet fission discovered in a disordered acene film. *J. Am. Chem. Soc.* **2012,** 134, 6388–6400.

33 Jadhav, P. J.; Brown, P. R.; Thompson, N.; Wunsch, B.; Mohanty, A.; Yost, S. R.; Hontz, E.; Voorhis, T. Van; Bawendi, M. G.; Bulović, V.; *et al*. Triplet exciton dissociation in singlet exciton fission photovoltaics. *Adv. Mater*. **2012,** 24, 6169–6174.

34 Wolf, E. A.; Finton, D. M.; Zoutenbier, V.; Biaggio, I. Quantum beats of a multiexciton state in rubrene single crystals. *Appl. Phys. Lett.* **2018,** 112, 083301.

35 Wang, X.; Garcia, T.; Monaco, S.; Schatschneider, B.; Marom, N. Effect of crystal packing on the excitonic properties of rubrene polymorphs. *CrystEngComm* **2016,** 18, 7353–7362.

36 Sharifzadeh, S.; Darancet, P.; Kronik, L.; Neaton, J. B. Low-energy charge-transfer excitons in organic solids from first-principles: the case of pentacene. *J. Phys. Chem. Lett*. **2013,** 4, 2197–2201.

37 Arias, D. H.; Ryerson, J. L.; Cook, J. D.; Damrauer, N. H.; Johnson, J. C. Polymorphism influences singlet fission rates in tetracene thin films. *Chem. Sci*. **2016,** 7, 1185–1191.

38 Bhattacharyya, K.; Datta, A. Polymorphism controlled singet fission in TIPS-anthracene: role of stacking orientation. *J. Phys. Chem. C* **2017,** 121, 1412–1420.

39 Wang, X.; Liu, X.; Cook, C.; Schatschneider, B.; Marom, N. On the possibility of singlet fission in crystalline quaterrylene. *J. Chem. Phys.* **2018,** 148, 184101.

40 Sutton, C.; Tummala, N. R.; Beljonne, D.; Brédas, J.-L. Singlet fission in rubrene derivatives: impact of molecular packing. *Adv. Mater.* **2017,** 29, 2777–2787.

41 Wang, L.; Olivier, Y.; Prezhdo, O. V.; Beljonne, D. Maximizing singlet fission by intermolecular packing. *J. Phys. Chem. Lett.* **2014,** 5, 3345–3353.

42 Feng, X.; Kolomeisky, A. B.; Krylov, A. I. Dissecting the effect of morphology on the rates of singlet fission: insights from theory. *J. Phys. Chem. C* **2014,** 118, 19608–19617.

43 Holmes, D.; Kumaraswamy, S.; Matzger, A. J.; Vollhardt, K. P. C. On the nature of nonplanarity in the [N]phenylenes. *Chem. – Eur. J.* **1999,** 5, 3399–3412.

44 Kitamura, C.; Matsumoto, C.; Kawatsuki, N.; Yoneda, A.; Kobayashi, T.; Naito, H. Crystal structure of 5,12-diphenyltetracene. *Anal. Sci.* **2006,** 22, x5–x6.

45 Jurchescu, O. D.; Meetsma, A.; Palstra, T. T. M. Low-temperature structure of rubrene single crystals grown by vapor transport. *Acta Cryst. B* **2006,** 62, 330–334.

46 Campbell, R. B.; Robertson, J. M.; Trotter, J. The crystal structure of hexacene, and a revision of the crystallographic data for tetracene. *Acta Cryst.* **1962,** 15, 289–290.

47 Miao, Q.; Chi, X.; Xiao, S.; Zeis, R.; Lefenfeld, M.; Siegrist, T.; Steigerwald, M. L.; Nuckolls, C. Organization of acenes with a cruciform assembly motif. *J. Am. Chem. Soc.* **2006,** 128, 1340–1345.

48 Schatschneider, B.; Phelps, J.; Jezowski, S. A new parameter for classification of polycyclic aromatic hydrocarbon crystalline motifs: a Hirshfeld surface investigation. *CrystEngComm* **2011,** 13, 7216–7223.

49 Schatschneider, B.; Monaco, S.; Liang, J.-J.; Tkatchenko, A. High-throughput investigation of the geometry and electronic structures of gas-phase and crystalline polycyclic aromatic hydrocarbons. *J. Phys. Chem. C* **2014,** 118, 19964–19974.

50 Hammouri, M.; Garcia, T. M.; Cook, C.; Monaco, S.; Jezowski, S.; Marom, N.; Schatschneider, B. High-throughput pressure-dependent density functional theory investigation of herringbone polycyclic aromatic hydrocarbons: part 1. pressure-dependent structure trends. *J. Phys. Chem. C* **2018,** 122, 23815–23827.

51 Hammouri, M.; Garcia, T. M.; Cook, C.; Monaco, S.; Jezowski, S.; Marom, N.; Schatschneider, B. High-throughput pressure-dependent density functional theory investigation of herringbone polycyclic aromatic hydrocarbons: part 2. pressure-dependent electronic properties. *J. Phys. Chem. C* **2018,** 122, 23828–23844.

52 Schatschneider, B.; Monaco, S.; Tkatchenko, A.; Liang, J.-J. Understanding the structure and electronic properties of molecular crystals under pressure: application of dispersion corrected DFT to oligoacenes. *J. Phys. Chem. A* **2013,** 117, 8323–8331.

53 Hybertsen, M. S.; Louie, S. G. Electron correlation in semiconductors and insulators: band gaps and quasiparticle energies. *Phys. Rev. B* **1986,** 34, 5390.

54 Rohlfing, M.; Louie, S. G. Electron-hole excitations and optical spectra from first principles. *Phys. Rev. B* **2000,** 62, 4927.

55 Marom, N. Accurate description of the electronic structure of organic semiconductors by *GW* methods. *J. Phys.: Condens. Matter* **2017,** 29, 103003.

56 Perdew, J. P.; Burke, K.; Ernzerhof, M. Generalized gradient approximation made simple. *Phys. Rev. Lett*. **1996,** 77, 3865–3868.

57 Perdew, J. P.; Burke, K.; Ernzerhof, M. Generalized gradient approximation made simple [Phys. Rev. Lett. 77, 3865 (1996)]. *Phys. Rev. Lett*. **1997,** 78, 1396.

58 Tkatchenko, A.; Scheffler, M. Accurate molecular van der Waals interactions from ground-state electron density and free-atom reference data. *Phys. Rev. Lett*. **2009,** 102, 073005.

59 Blum, V.; Gehrke, R.; Hanke, F.; Havu, P.; Havu, V.; Ren, X.; Reuter, K.; Scheffler, M. *Ab initio* molecular simulations with numeric atom-centered orbitals. *Comput. Phys. Commun*. **2009,** 180, 2175–2196.

60 Havu, V.; Blum, V.; Havu, P.; Scheffler, M. Efficient O(N) integration for all-electron electronic structure calculation using numeric basis functions. *J. Comput. Phys*. **2009,** 228, 8367–8379.

61 Ren, X.; Sanfilipo, A.; Rinke, P.; Wieferink, J.; Tkatchenko, A.; Reuter, K.; Blum, V.; Scheffler, M. Resolution-of-identity approach to Hartree–Fock, hybrid density functionals, RPA, MP2 and *GW* with numeric atom-centered orbital basis functions. *New J. Phys*. **2012,** 14, 053020.

62 Sutton, C.; Marshall, M. S.; Sherrill, C. D.; Risko, C.; Brédas, J.-L. Rubrene: the interplay between intramolecular and intermolecular interactions determines the planarization of its tetracene core in the solid state. *J. Am. Chem. Soc*. **2015,** 137, 8775–8782.

63 Casanova, D. Electronic structure study of singlet fission in tetracene derivatives. *J. Chem. Theory Comput*. **2014,** 10, 324–334.

64 Knight, J. W.; Wang, X.; Gallandi, L.; Dolgounitcheva, O.; Ren, X.; Ortiz, J. V.; Rinke, P.; Korzdorfer, T.; Marom, N. Accurate ionization potentials and electron affinities of acceptor molecules III: a benchmark of *GW* methods. *J. Chem. Theory Comput*. **2016,** 12, 615–626.

65 Deslippe, J.; Samsonidze, G.; Strubbe, D. A.; Jain, M.; Cohen, M. L.; Louie, S. G. BerkeleyGW: a massively parallel computer package for the calculation of the quasiparticle and optical properties of materials and nanostructures. *Comput. Phys. Commun*. **2012,** 183, 1269.

66 Jacquemin, D.; Duchemin, I.; Blondel, A.; Blase, X. Benchmark of Bethe-Salpeter for triplet excited-states. *J. Chem. Theory Comput.* **2017,** 13, 767–783.

67 Rangel, T.; Hamed, S. M.; Bruneval, F.; Neaton, J. B. An assessment of low-lying excitation energies and triplet instabilities of organic molecules with an *ab initio* Bethe-Salpeter equation approach and the Tamm-Dancoff approximation. *J. Chem. Phys.* **2017,** 146, 194108.

68 Ziaei, V.; Bredow, T. Simple many-body based screening mixing ansatz for improvement of *GW*/Bethe-Salpeter equation excitation energies of molecular systems. *Phys. Rev. B* **2017,** 96, 195115.

69 Ziaei, V.; Bredow, T. Screening mixing *GW*/Bethe-Salpeter approach for triplet states of organic molecules. *J. Phys.: Condens. Matter* **2018,** 30, 395501.

70 Clark, S. J.; Segall, M. D.; Pickard, C. J.; Hasnip, P. J.; Probert, M. J. J.; Refson, K.; Payne, M. C. First principles methods using CASTEP. *Z. Kristallogr. – Cryst. Mater.* **2005,** 220, 567.

71 Giannozzi, P.; Baroni, S.; Bonini, N.; Calandra, M.; Car, R.; Cavazzoni, C.; Ceresoli, D.; Chiarotti, G. L.; Cococcioni, M.; Dabo, I.; *et al*. QUANTUM ESPRESSO: a modular and open-source software project for quantum simulations of materials. *J. Phys.: Condens. Matter* **2009,** 21, 395502.

72 Deslippe, J.; Samsonidze, G.; Jain, M.; Cohen, M. L.; Louie, S. G. Coulomb-hole summations and energies for *GW* calculations with limited number of empty orbitals: a modified static remainder approach. *Phys. Rev. B* **2013,** 87, 165124.

73 Tang, W.; Sanville, E.; Henkelman, G. A grid-based Bader analysis algorithm without lattice bias. *J. Phys.: Condens. Matter* **2009,** 21, 084204.

74 Sharifzadeh, S.; Biller, A.; Kronik, L.; Neaton, J. B. Quasiparticle and optical spectroscopy of the organic semiconductors pentacene and PTCDA from first principles. *Phys. Rev. B* **2012,** 85, 125307.

75 Simon, Y. C.; Weder, C. Low-power photon upconversion through triplet-triplet annihilation in polymers. *J. Mater. Chem*. **2012,** 22, 20817–20830.

76 Schulze, T. F.; Schmidt, T. W. Photochemical upconversion: present status and prospects for its application to solar energy conversion. *Energy Environ. Sci*. **2015,** 8, 103–125.

77 Dzebo, D.; Börjesson, K.; Gray, V.; Moth-Poulsen, K.; Albinsson, B. Intramolecular triplet-triplet annihilation upconversion in 9,10-diphenylanthracene oligomers and dendrimers. *J. Phys. Chem. C* **2016,** 120, 23397–23406.

78 Schatschneider, B.; Liang, J.-J.; Reilly, A. M.; Marom, N.; Zhang, G.-X.; Tkatchenko, A. Electrodynamic response and stability of molecular crystals. *Phys. Rev. B* **2013,** 87, 060104(R).

79 Marom, N.; Körzdörfer, T.; Ren, X.; Tkatchenko, A.; Chelikowsky, J. R. Size effects in the interface level alignment of dye-sensitized TiO_2 clusters. *J. Phys. Chem. Lett*. **2014,** 5, 2395–2401.

80 Tkatchenko, A.; DiStasio Jr., R. A.; Car, R.; Scheffler, M. Accurate and efficient method for many-body van der Waals interactions. *Phys. Rev. Lett*. **2012,** 108, 236402.

81 Hill, I. G.; Kahn, A.; Soos, Z. G.; Pascal Jr, R. A. Charge-separation energy in films of π-conjugated organic molecules. *Chem. Phys. Lett.* **2000,** 327, 181–188.

82 Sato, N.; Seki, K.; Inokuchi, H. The kinetics of the solvolysis of the 1,2-chloroazido-bus(ethylenediamine)cobalt(III) ion in water and in water + isopropanol. *J. Chem. Soc., Faraday Trans. 1* **1981,** 77, 1621–1628.

83 Li, J.; D'Avino, G.; Duchemin, I.; Beljonne, D.; Blase, X. Combining the many-body *GW* formalism with classical polarizable models: insights on the electronic structure of molecular solids. *J. Phys. Chem. Lett.* 2016, 7, 2814–2820.

84 van Setten, M. J.; Caruso, F.; Sharifzadeh, S.; Ren, X.; Scheffler, M.; Liu, F.; Lischner, J.; Lin, L.; Deslippe, J. R.; Louie, S. G.; *et al*. *GW*100: benchmarking G_0W_0 for molecular systems. *J. Chem. Theory Comput.* **2015,** 11, 5665–5687.

85 Huang, L.; Liao, Q.; Shi, Q.; Fu, H.; Ma, J.; Yao, J. Rubrene micro-crystals from solution routes: their crystallography, morphology and optical properties. *J. Mater. Chem.* **2010,** 20, 159–166.

86 Leng, X.; Feng, J.; Chen, T.; Liu, C.; Ma, Y. Optical properties of acene molecules and pentacene crystal from the many-body Green's function method. *Phys. Chem. Chem. Phys.* **2016,** 18, 30777–30784.

87 Bruneval, F.; Hamed, S. M.; Neaton, J. B. A systematic benchmark of the *ab initio* Bethe–Salpeter equation approach for low-lying optical excitations of small organic molecules. *J. Chem. Phys*. **2015,** 142, 244101.

88 Jacquemin, D.; Duchemin, I.; Blase, X. Benchmarking the Bethe–Salpeter formalism on a standard organic molecular set. *J. Chem. Theory Comput*. **2015,** 11, 3290–3304.

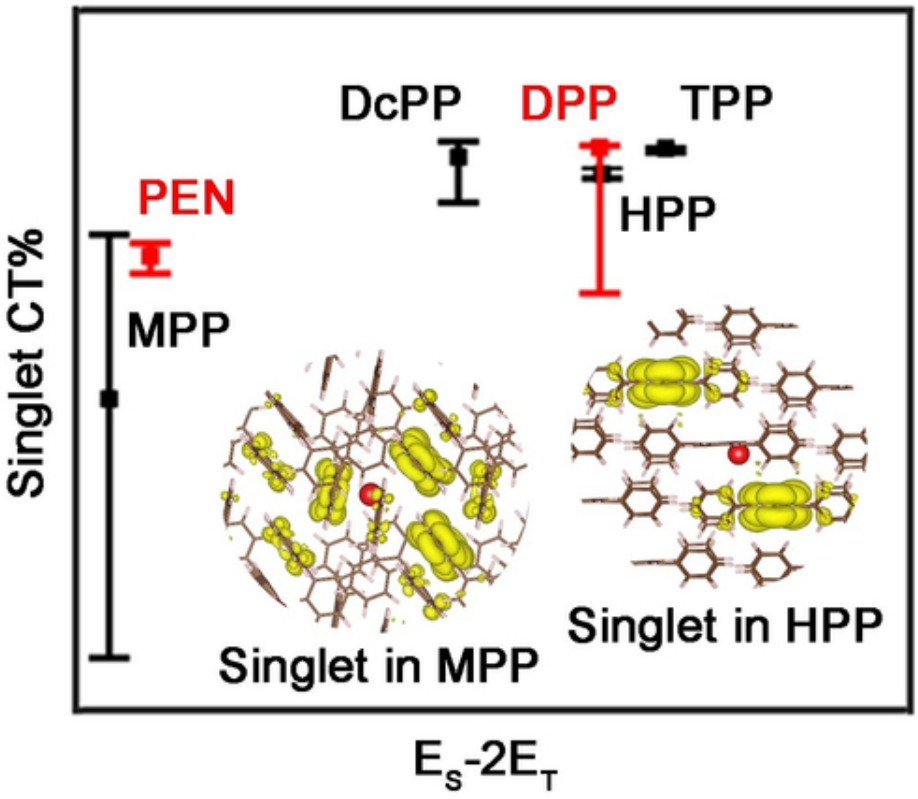

TOC graphic

45x39mm (300 x 300 DPI)

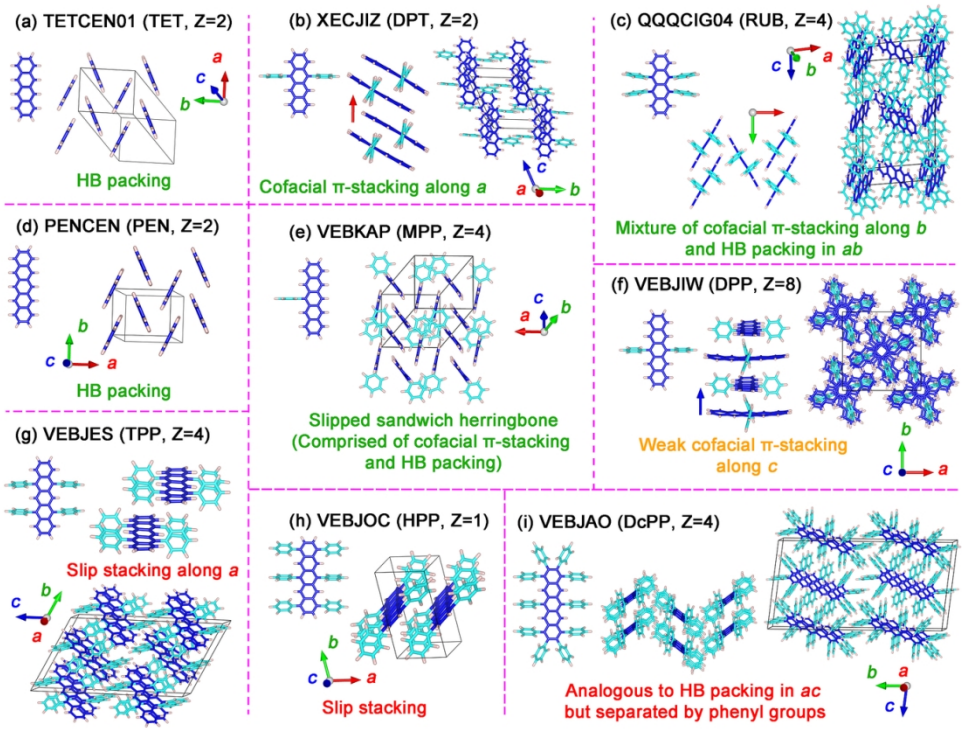

Figure 1

119x90mm (300 x 300 DPI)

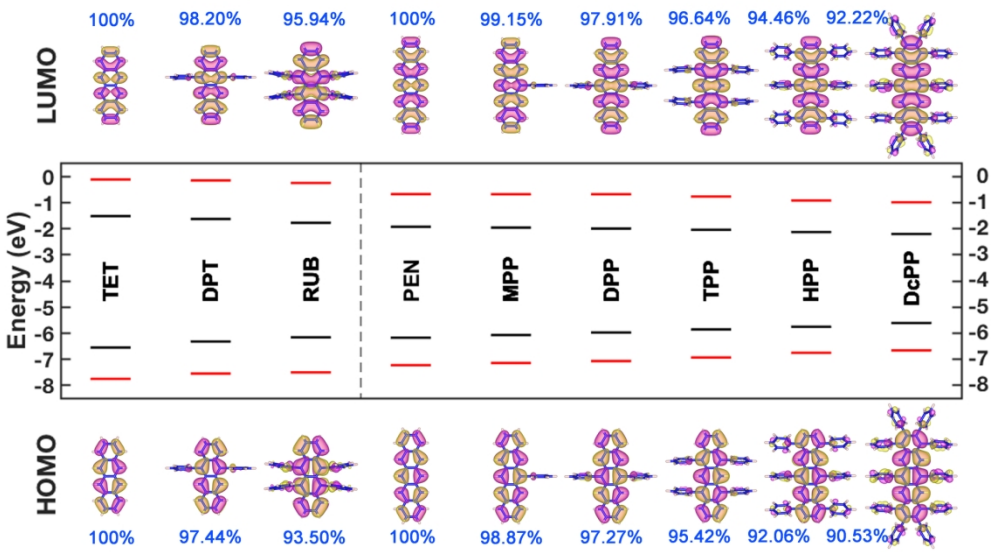

Figure 2

160x90mm (300 x 300 DPI)

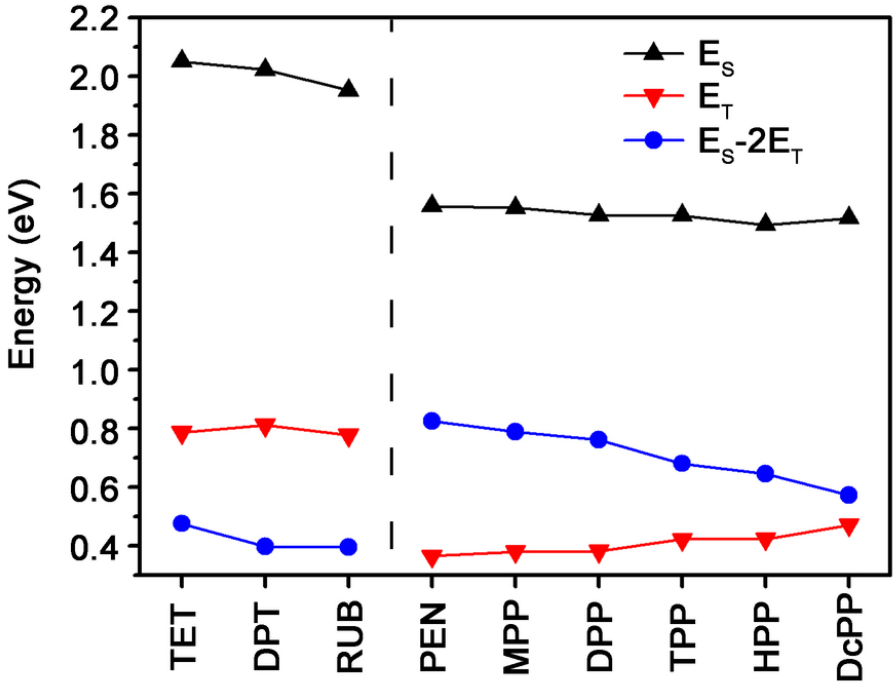

Figure 3

82x59mm (300 x 300 DPI)

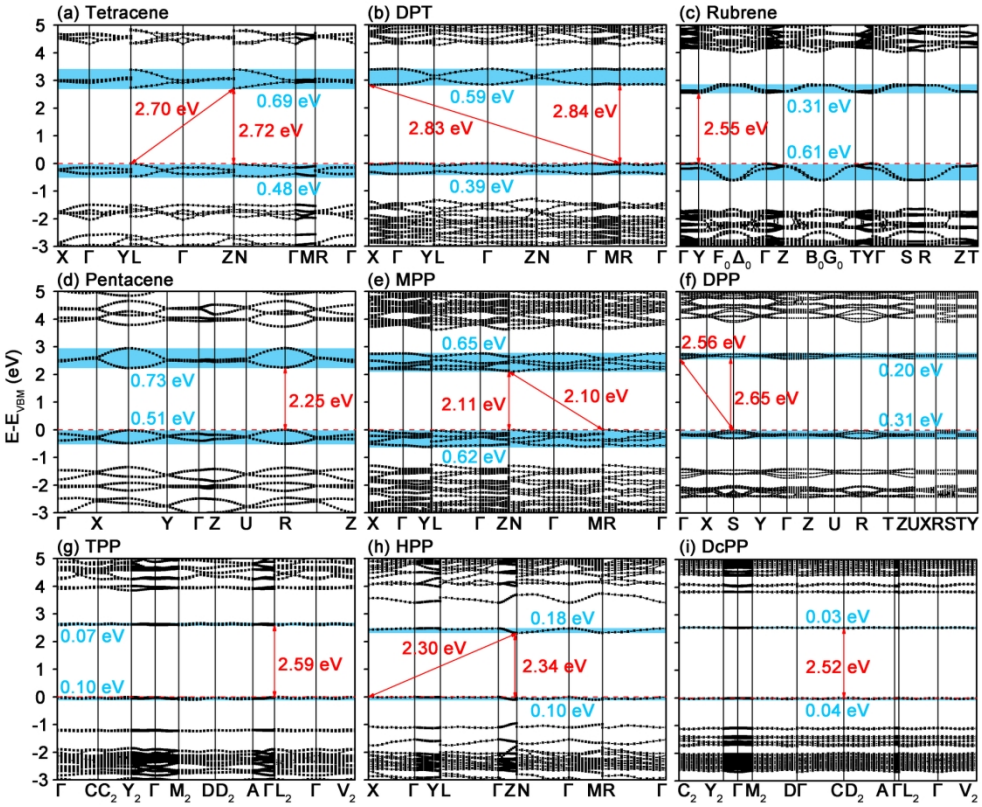

Figure 4

160x130mm (300 x 300 DPI)

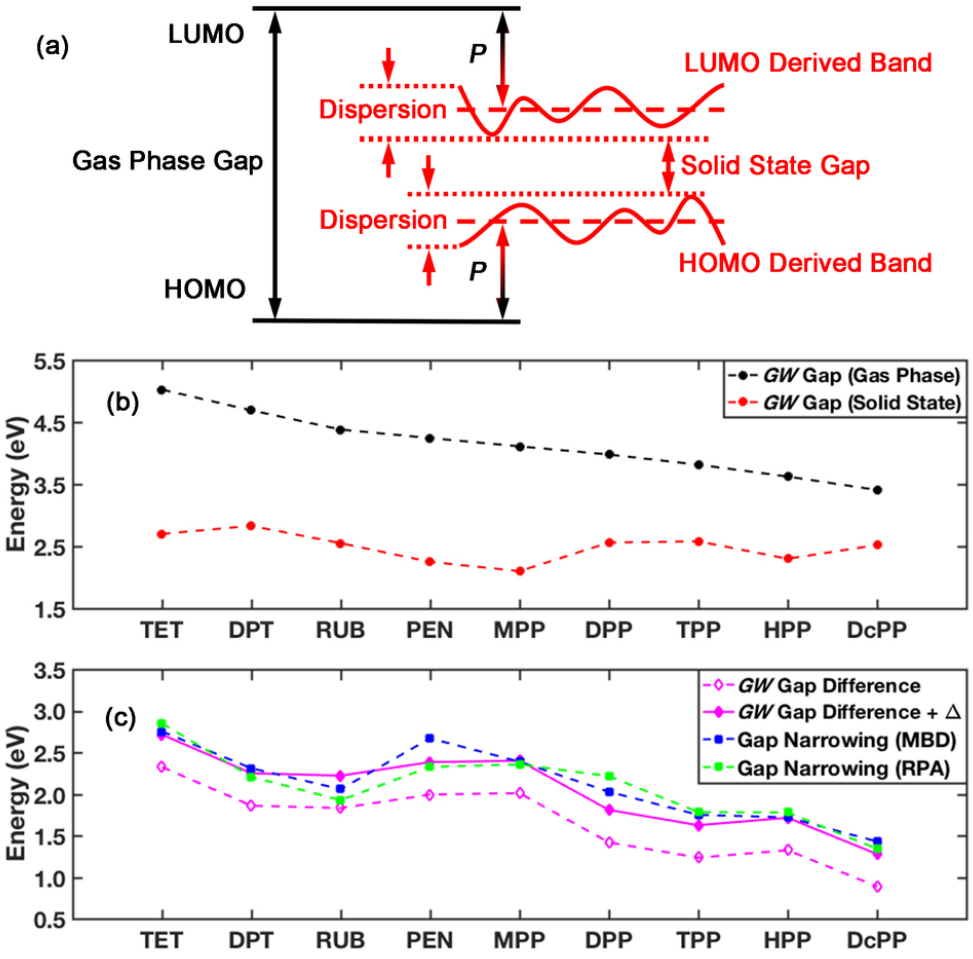

Figure 5

82x82mm (300 x 300 DPI)

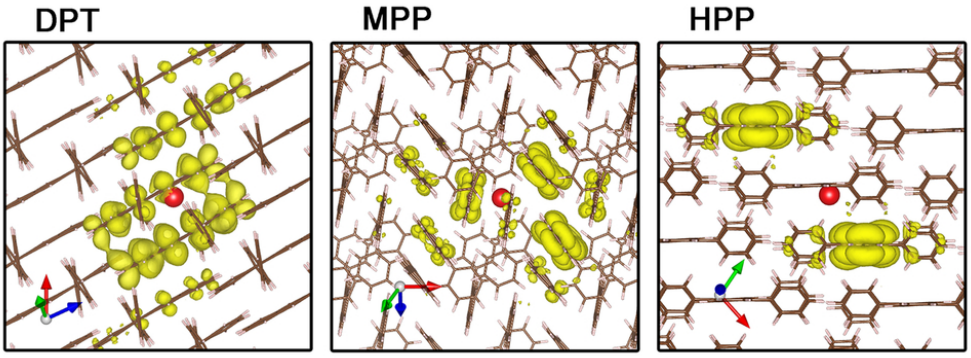

Figure 6

82x34mm (300 x 300 DPI)

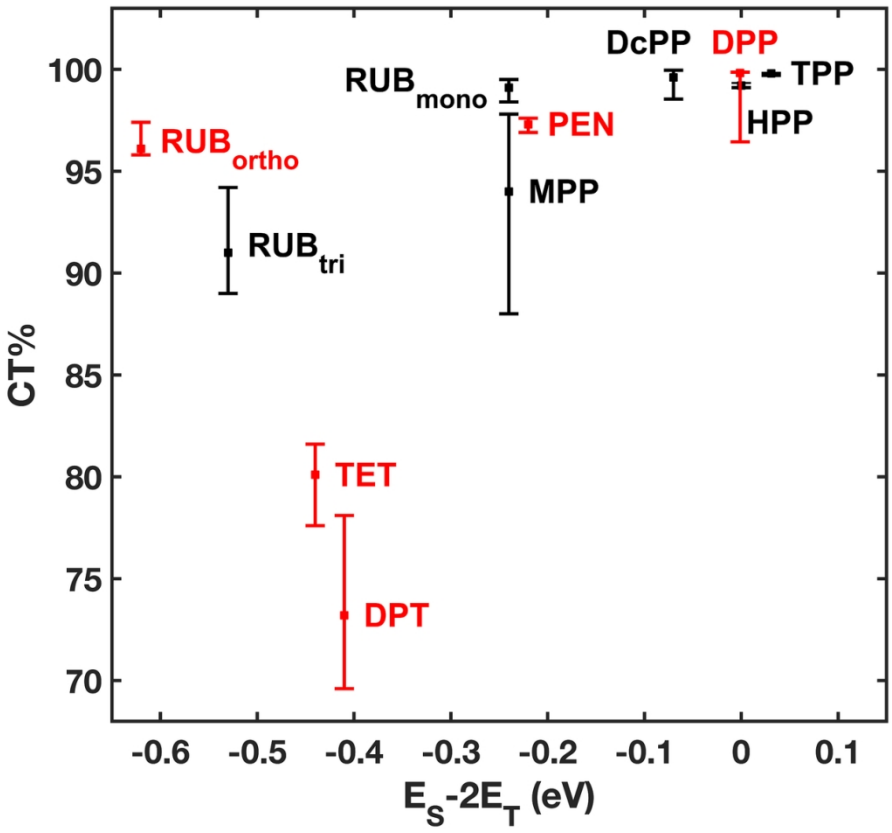

Figure 7

119x106mm (300 x 300 DPI)